

Article

Observation of Distinct Two-Photon Transition Channels in CdTe Quantum Dots in a Regime of Very Strong Confinement

Marcelo Gonçalves Vivas^{1,2,*}, José Carlos Leandro De Sousa³, Leonardo De Boni²,
Marco Antônio Schiavon³ and Cleber Renato Mendonca^{2,*}

¹ Instituto de Ciência e Tecnologia, Universidade Federal de Alfenas, Poços de Caldas, Minas Gerais 37715-400, Brazil

² Instituto de Física de São Carlos, Universidade de São Paulo, São Carlos, São Paulo 13560-970, Brazil; deboni@ifsc.usp.br

³ Departamento de Ciências Naturais, Universidade Federal de São João del-Rei, São João del-Rei, Minas Gerais 36301-160, Brazil; jclsousa27@gmail.com (J.C.L.D.S.); schiavon@ufsj.edu.br (M.A.S.)

* Correspondence: mavivas82@gmail.com (M.G.V.); crmendon@ifsc.usp.br (C.R.M.); Tel.: +55-35-3697-4755 (M.G.V.); +55-16-3373-8085 (ext. 236) (C.R.M.)

Academic Editor: Qing-Hua Xu

Received: 20 January 2017; Accepted: 23 March 2017; Published: 30 March 2017

Abstract: We report here on the direct observation of distinct two-photon transition channels in glutathione-capped (GSH) CdTe quantum dots (QDs) in a very strong confinement regime. CdTe-GSH QDs with different average diameters (2.5, 3.0, and 3.3 nm) were synthesized through the one-pot method and their two-photon absorption (2PA) spectrum determined by a femtosecond wavelength-tunable Z-scan. Our results show that the two lower-energy one-photon-allowed excitonic transitions, $1S_{3/2}(h) \rightarrow 1S(e)$ and $2S_{3/2}(h) \rightarrow 1S(e)$, are also accessed via 2PA. These results were ascribed to the relaxation of the parity selection rules due to the noncentrosymmetric structure of the CdTe QDs (zinc-blended structure), whose magnitude are determined by surface defects and structural irregularities present in CdTe-GSH QDs, in the strong confinement regime.

Keywords: CdTe quantum dots; 2PA transition channels; femtosecond two-photon spectroscopy

1. Introduction

Semiconductor quantum dots (QDs) are nanomaterials represented by a three-dimensionally confined electron-hole system. Such tight spatial confinement provides interesting optical features, such as size-tunable absorption and emission, which are closely associated with new technologies spanning from biology to physics [1–15].

The optical properties of QDs are described by quantum mechanics, being hence subjected to its selection rules [16,17]. Therefore, to describe the selection rules and to unveil the electronic structure of these materials, it is necessary to know the wave-functions symmetry, which defines the parity of the electronic states. The symmetry of each electronic state is expressed by their quantum numbers (principal (n), azimuthal (l), and magnetic (m_l)), which dictates the electron-hole recombination induced by single or multi-photons absorption. Materials exhibiting inversion symmetry, such as PbS and PbSe QDs, present antagonistic dipole electric allowed transitions induced by one-photon absorption (1PA) and two-photon absorption (2PA), i.e., one-photon-allowed states are forbidden by 2PA and vice versa. Therefore, while the electron-hole recombination excited by 2PA occurs between states satisfying $\Delta l = l_e - l_h = \pm 1$ (subscript e and h corresponds to electron and hole, respectively), in one-photon-induced transitions, it occurs only if $\Delta l = l_e - l_h = 0$ [16,17]. Some mechanisms, however, can break the inversion symmetry of the wave functions that describe the

electronic states. For example, interactions with a solvent, the Stark transient effect, a magnetic field, surface defects, and structural irregularities, among others, may prevent the wave function from presenting a well-defined parity [17–21]. In this context, one-photon-allowed states may also be accessed via 2PA. However, it is worth mentioning that 2PA-allowed transition probability is strongly dependent on the state symmetry degree. Therefore, broadband analysis of the 2PA spectrum in QDs can provide important information about the electronic and structural features of such nanomaterials.

II–VI semiconductor quantum dots have been shown to present a high 2PA cross section (expressed in GM = 10^{-50} cm⁴ s⁻¹ photon⁻¹) along the visible and near-infrared regions. Among them, it is worth highlighting ZnS (~200 GM at 600 nm, diameter = 3.8 nm [22]), CdS (4.4×10^3 GM at 800 nm, diameter = 4.45 nm [23]), CdSe (2×10^4 GM at 950 nm; diameter = 3.7 nm [24]), CdTe ($\sim 3.0 \times 10^3$ GM at 900 nm, diameter = 4 nm [25]), and PbS (6×10^4 GM at 1460 nm, diameter = 3.7 nm [26]) QDs.

CdTe QDs with a zinc-blended structure (cubic T_d structure), as the ones studied here, are noncentrosymmetric semiconductors [27]; therefore, to model the entire 2PA spectra, an additional transition channel should be taken into account, in which the quantum numbers are conserved analogously to the one-photon-allowed transitions, i.e., $\Delta l = 0$, the so-called noncentrosymmetric 2PA transition channel. Figure 1 illustrates the energy diagram for the lower-energy 1PA- and 2PA-allowed transitions for CdTe QDs.

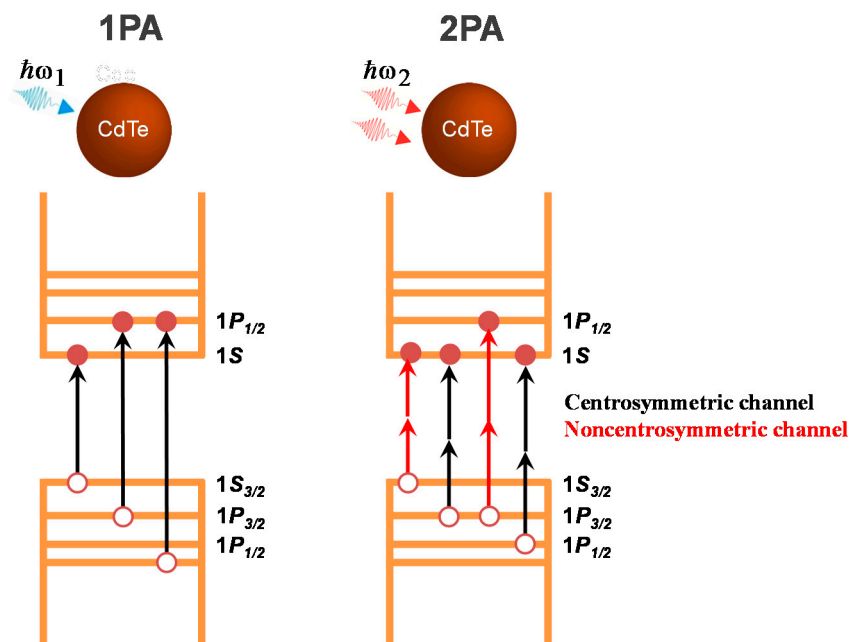


Figure 1. Energy diagram for the lowest energy 1PA- and 2PA-allowed transitions for quantum dots (QDs).

Fedorov et al. [16] deduced an analytical expression for the 2PA cross section containing centrosymmetric and noncentrosymmetric channels, by using the parabolic effective mass approximation. Although this model describes reasonably well the 2PA spectrum for CdS and CdSe QDs in the regime of intermediate confinement, as reported in Refs. [16,22,28], it fails to describe the 2PA-allowed optical transition when CdTe QDs are in a very strong confinement regime, as shown in Ref. [25]. The discrepancy between the experimental and theoretical (Fedorov's model) data is even higher for CdTe QDs due to its effective mass values for electron and holes (light, heavy, and split-off). Furthermore, the parabolic effective mass approximation presents some limitations: (i) the zero-order approximation of the Hamiltonian for regions where $\vec{k} \sim 0$; (ii) the fact that the model does not consider mixing among the heavy- and the light-hole bands; (iii) the fact that the effective masses are considered constants (parabolic bands) [29].

Although some studies reported 2PA properties of CdTe QDs [25,29–32], few present nonlinear spectra in a broad spectral region using femtosecond laser pulses. Furthermore, works on the 2PA in CdTe QDs do not mention the possibility of a contribution from the noncentrosymmetric channel to the 2PA cross section in the very strong confinement regime. For example, Padilha et al. [32] reports on the noncentrosymmetric channel for the 2PA cross section of CdTe QDs in glass matrices in the intermediate confinement regime (diameter higher than 6 nm, Bohr radius for CdTe is 7.5 nm [29]). Even so, the reported degenerate 2PA spectrum, for CdTe QDs does not include the region for the lowest energy transition ($1S_{3/2}(h) \rightarrow 1S(e)$), and the available data are limited to specific wavelengths. In the same way, Qu et al. [25] reported a spherical eight-band Pidgen and Brown model that considers the mixing between the conduction and the valence bands, as well as the complex structure of the valence bands. However, this model exhibits only 2PA transitions that are governed by the electric-dipole selection rules; therefore, it does not consider the “forbidden” 2PA transition, such as the $1S_{3/2}(h) \rightarrow 1S(e)$ lowest-energy excitonic transition. In this context, this work reports on the femtosecond 2PA cross-section spectra of water soluble colloidal CdTe-GSH QDs in the very strong confinement regime, emphasizing the influence of the noncentrosymmetric 2PA transition channel. For that, we reported the broadband 2PA cross-section spectra from 600 nm to 1220 nm, in 10 nm intervals, providing high spectral resolution to the nonlinear measurements.

2. Results and Discussion

Figure 2 depicts the one- and two-photon absorption spectra for three CdTe-GSH samples with different average diameters (\bar{D}), within the regime of strong quantum confinement, namely CdTe-507 ($\bar{D} = 2.5 \text{ nm}$), CdTe-531 ($\bar{D} = 3.0 \text{ nm}$), and CdTe-554 ($\bar{D} = 3.3 \text{ nm}$). The 1PA spectra (solid lines, left axis) exhibit the well-defined first $1S_{3/2}(h) \rightarrow 1S(e)$ excitonic transition (lowest energetic band). This transition undergoes a red-shift of approximately 200 meV when CdTe-507 is compared to CdTe-554, indicating an increase in QD size [33]. By using the Yu’s formula for CdTe QDs [34], the average diameter for each CdTe-GSH QDs is estimated to be 2.5 nm, 3.0 nm, and 3.3 nm. CdTe-GSH QDs optical properties, such as molar absorptivity (ϵ_{1PA}), fluorescence maximum position (FMP), fluorescence lifetime (τ_f), relative fluorescence quantum yield (ϕ_f), as well as parameter obtained from the 2PA spectra are shown in Table 1. It is important to mention that the QDs samples exhibit spherical shapes and size dispersion of approximately 25 %, as determined by Transmission Electron Microscopy analysis.

In Figure 2, the symbols along the line (right axis) display the 2PA cross section for CdTe-GSH QDs as a function of half of the excitation wavelength, to provide better comparison with the 1PA. As it can be seen, the 2PA spectra present three defined peaks as labeled on the figure, which are superimposed by the intermediate state resonance enhancement effect (ISRE), described by the monotonic decrease on the 2PA cross section from the UV to the red region. In the ISRE UV region, the 2PA cross section reaches extremely high values, from $6.0 \times 10^3 \text{ GM}$ (CdTe-507) up to $\sim 1.8 \times 10^4 \text{ GM}$ (CdTe-554). It occurs because the excitation photon energy approaches the first 1PA-allowed transition, increasing the 2PA cross section. [26] Moreover, the higher number of excited states contributing to the 2PA process also increases the 2PA cross section as the excitation energy increases [16]. One can observe that, in the lowest energy 2PA peaks, labeled as 1st in Figure 2, 2PA cross-section values range from $1.6 \times 10^3 \text{ GM}$ (CdTe-507—Figure 2a) to $2.9 \times 10^3 \text{ GM}$ (CdTe-554—Figure 2c). Moreover, an important feature of this state, observed in this work, is that it is allowed by one- and two-photon absorption, indicating that the $1S_{3/2}(h) \rightarrow 1S(e)$ transition has its electric-dipole selection rules relaxed.

A few years ago, the 2PA cross-section spectra for CdTe QDs were investigated in Refs. [25,29] using, respectively, the $\vec{k} \cdot \vec{p}$ model, including the mixing among the heavy- and light-hole bands, and the spherical eight-band Pidgen and Brown model [27], which considers the mixing between the conduction and the valence bands as well as the complex structure of the valence bands. However, in both studies, the correspondence between 1PA and 2PA transitions was not observed, indicating a discrepancy with our experimental results. In order to visualize it, in Figure 3a, we compare the

experimental 2PA spectrum we obtained (dots) for the CdTe-531 ($D = 3.0$ nm) with theoretical data obtained from Ref. [25] (solid line).

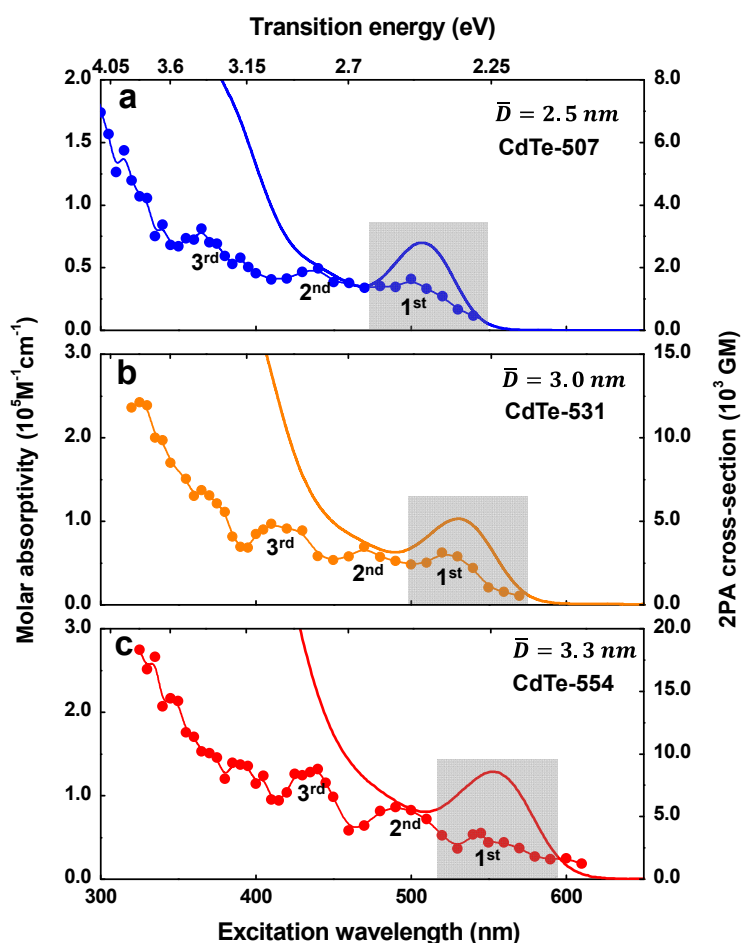


Figure 2. One-photon absorption (1PA) (solid lines, left axis) and two-photon absorption (2PA) (symbols, right axis) spectra for CdTe-GSH QDs (a) CdTe-507; (b) CdTe-531 and (c) CdTe-554. The standard deviation for the 2PA cross section is about 10%.

Based on Figure 3a, two important differences between the experimental and theoretical spectrum can be highlighted. The first one is that the 2PA cross sections for the experimental data are slightly higher than theoretical ones. The second one is that the experimental 2PA spectrum presents more 2PA transitions as compared to the theoretical data. Moreover, such two aspects are closely related because the increase in the number of transitions tends to enhance the 2PA cross section. At the same time, both differences should be associated with the noncentrosymmetric 2PA transition channel due to cubic zinc-blended structure with T_d symmetry of the CdTe QDs. To aid in the understanding of these important outcomes, in Figure 3b, the difference between the experimental and theoretical 2PA spectrum were plotted, which allows for the obtainment of information about the noncentrosymmetric 2PA transitions. Proceeding in this way, one can note that the two lower-energy 1PA-allowed transitions, i.e., the $1S_{3/2}(h) \rightarrow 1S(e)$ (peak at 2.32 eV) and $2S_{3/2}(h) \rightarrow 1S(e)$ (peak at 2.62 eV), are observed along to the 2PA spectrum, corroborating our previous analysis. Higher energy transitions are also observed in Figure 3b, but they cannot be separately identified because of the large number of transitions in this spectral region.

Table 1. Optical properties of CdTe-GSH QDs.

\bar{D} (nm)	1PA Peak (eV)	ϵ (10^5 $M^{-1}cm^{-1}$)	ϕ_f	FMP (eV)	τ_f (ns)	2PA Cross-Section (10^3 GM)	FOM (GM/nm^3)	2PA Transition (eV)
2.5	2.45 (507 nm)	0.70	0.13	2.27 (547 nm)	35	1 st \rightarrow 1.60	196	2.45
						2 nd \rightarrow 1.97	240	2.82
						3 rd \rightarrow 3.24	396	3.40
3.0	2.34 (531 nm)	1.01	0.16	2.15 (576 nm)	43	1 st \rightarrow 3.12	220	2.34
						2 nd \rightarrow 3.46	245	2.64
						3 rd \rightarrow 4.55	322	3.00
3.3	2.24 (554 nm)	1.27	0.29	2.07 (599 nm)	50	1 st \rightarrow 2.92	155	2.24
						2 nd \rightarrow 5.65	300	2.50
						3 rd \rightarrow 8.54	454	2.85

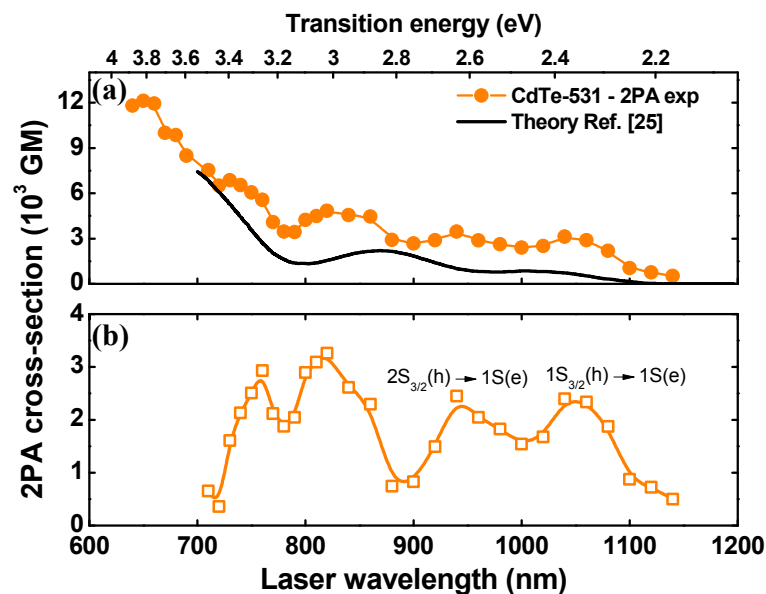


Figure 3. (a) Experimental (dots) and theoretical (solid line, data from the Ref. [25]) 2PA spectrum for CdTe-GSH QDs (CdTe-531); (b) The difference between the experimental and theoretical 2PA spectrum reported in part (a).

Therefore, these results confirm that parity selection rules were relaxed for the CdTe-GSH QDs samples, presented here. Another interesting feature that can be observed in Figure 2 is that the 2PA strength for the $1S_{3/2}(h) \rightarrow 1S(e)$ transition normalized by the QD volume decreases with larger QDs. More specifically, the 2PA figure of merit (FOM), defined as the 2PA cross sections divided by the QD volume, decrease from $196 \text{ GM}/\text{nm}^3$ ($\bar{D} = 2.5 \text{ nm}$) to $154 \text{ GM}/\text{nm}^3$ ($\bar{D} = 3.3 \text{ nm}$).

This result is attributed to a decrease in surface defects and improvement of the structural regularity for larger CdTe-GSH QDs. In fact, the fluorescence quantum yield for these samples rise as a function of QD size (see Table 1) due to a better QDs surface quality ascribed to the Ostwald ripening mechanism [35]. In this process, an increase in the synthesis time causes the dissolution of smaller QDs, which precipitate onto the surface of larger QDs. As a consequence, the average QD size increases causing an increase in the surface quality and structural regularity of nanocrystals.

In Figure 2, the 2PA spectra exhibits two higher-energy peaks, labeled as 2nd and 3rd, with a 2PA cross section ranging from 1.97×10^3 to 5.65×10^3 GM. The magnitude of these 2PA peaks are in the same order of those published in Ref. [25,29,32], indicating that the 2PA cross section in these regions are predominantly related to higher energy 2PA-allowed excitonic transitions. However, as shown in Figure 3b, a considerable contribution of the noncentrosymmetric 2PA transition channel was observed for the higher energy region of the 2PA spectrum. It is interesting to note that the FOM for the 2nd

and 3rd maxima increase with larger QDs, i.e., $FOM^{2nd} = 245 \text{ GM/nm}^3$ and $FOM^{3rd} = 322 \text{ GM/nm}^3$ for CdTe-507 and $FOM^{2nd} = 300 \text{ GM/nm}^3$ and $FOM^{3rd} = 454 \text{ GM/nm}^3$ for CdTe-554. This behavior corroborates our previous results because a reduction of surface defects leads to a decrease in the 2PA forbidden transition strength (as pointed by the FOM for the $1S_{3/2}(h) \rightarrow 1S(e)$), while it increases for 2PA-allowed transition, analogous to what occurs in organic chromophores [20,36].

3. Materials and Methods

We used the one-pot method, whose details can be found in Refs. [37,38], to synthesize glutathione-capped CdTe QDs. The linear and nonlinear optical measurements were performed in aqueous solutions of GSH-capped CdTe QDs, with concentrations on the order of 10^{16} QDs/cm^3 and 10^{17} QDs/cm^3 , respectively. The steady-state absorption and fluorescence spectra were recorded using a Shimadzu UV-1800 spectrophotometer (Shimadzu, Kyoto, Japan) and a Perkin Elmer LS55 fluorimeter (Waltham, MA, USA), respectively.

The fluorescence quantum yields (ϕ_f) of the nanocrystals were determined using the fluorescence spectrum of the samples, in a comparative method that uses the fluorescence spectrum and quantum yield of a reference sample [39]. Here, we used Rhodamine 6G dissolved in water as the standard fluorescent dye ($\phi_f = 92\%$).

Fluorescence lifetime was measured by exciting the CdTe QDs at 532 nm (frequency double of a Q-switched and mode-locked Nd:YAG—70 ps). The 532 nm beam was focused into the sample, placed in a 2-mm-thick fused silica cuvette, with a lens with a focal length of 12 cm. The fluorescence signal was collected perpendicularly to the excitation beam by an optical fiber positioned close to the fluorescent spot. The signal was acquired by a silicon photodetector with a rise time of approximately 0.5 ns and subsequently averaged and recorded with a digital oscilloscope (5 GS/s).

4. Final Remarks

The relaxation of the parity selection rules in noncentrosymmetric CdTe-GSH QDs at the very strong confinement regime was observed. Our results show a coincidence between 1PA and 2PA peaks, indicating that a one-photon transition is also allowed by two-photon excitation. To explain this, we considered that, due to the zinc-blended structure with T_d symmetry, CdTe QDs do not present inversion symmetry; therefore, the parity of the electronic states involved in optical transitions are not precisely defined. Thus, the coincidence between the lowest energy 1PA and 2PA peaks can be explained through the relaxation of the parity selection rules. In addition, we show that the reduction in surface defects and structural irregularities with the increase in QD size, very common in colloidal QD synthesis in the strong confinement regime, increases the centrosymmetric and decreases the noncentrosymmetric 2PA channel strength.

Acknowledgments: Financial support from FAPESP (Fundação de Amparo à Pesquisa do Estado de São Paulo—2011/12399-0 and 2015/20032-0), FAPEMIG (Fundação de Amparo à Pesquisa do Estado de Minas Gerais, APQ-01203-16), CNPq (Conselho Nacional de Desenvolvimento Científico e Tecnológico), Coordenação de Aperfeiçoamento de Pessoal de Nível Superior (CAPES), and the Air Force Office of Scientific Research (FA9550-12-1-0028 and FA9550-15-1-0521) are acknowledged.

Author Contributions: Marcelo Gonçalves Vivas, Leonardo De Boni, and Cleber Renato Mendonça conceived and designed the experiments; José Carlos Leandro de Sousa and Marco Antônio Schiavon synthesized the samples; Marcelo Gonçalves Vivas analyzed the data; Marcelo Gonçalves Vivas, Leonardo De Boni, and Cleber Renato Mendonça wrote the paper.

Conflicts of Interest: The authors declare no conflict of interest.

References

1. Alivisatos, A.P. Semiconductor Clusters, Nanocrystals, and Quantum Dots. *Science* **1996**, *271*, 933–937. [[CrossRef](#)]
2. Andersen, M.L.; Stobbe, S.; Sorensen, A.S.; Lodahl, P. Strongly Modified Plasmon-Matter Interaction with Mesoscopic Quantum Emitters. *Nat. Phys.* **2011**, *7*, 215–218. [[CrossRef](#)]

3. Anikeeva, P.O.; Halpert, J.E.; Bawendi, M.G.; Bulovic, V. Quantum Dot Light-Emitting Devices with Electroluminescence Tunable over the Entire Visible Spectrum. *Nano Lett.* **2009**, *9*, 2532–2536. [[CrossRef](#)] [[PubMed](#)]
4. Bakalova, R.; Ohba, H.; Zhelev, Z.; Nagase, T.; Jose, R.; Ishikawa, M.; Baba, Y. Quantum dot anti-CD conjugates: Are they potential photosensitizers or potentiators of classical photosensitizing agents in photodynamic therapy of cancer? *Nano Lett.* **2004**, *4*, 1567–1573. [[CrossRef](#)]
5. Bourzac, K. Quantum dots go on display. *Nature* **2013**, *493*, 283. [[CrossRef](#)] [[PubMed](#)]
6. Bratschitsch, R.; Leitenstorfer, A. Quantum dots: Artificial atoms for quantum optics. *Nat. Mater.* **2006**, *5*, 855–856. [[CrossRef](#)] [[PubMed](#)]
7. Chan, W.C.W.; Nie, S.M. Quantum dot bioconjugates for ultrasensitive nonisotopic detection. *Science* **1998**, *281*, 2016–2018. [[CrossRef](#)] [[PubMed](#)]
8. Dahan, M.; Laurence, T.; Pinaud, F.; Chemla, D.S.; Alivisatos, A.P.; Sauer, M.; Weiss, S. Time-gated biological imaging by use of colloidal quantum dots. *Opt. Lett.* **2001**, *26*, 825–827. [[CrossRef](#)] [[PubMed](#)]
9. Haverinen, H.M.; Myllyla, R.A.; Jabbour, G.E. Inkjet printing of light emitting quantum dots. *Appl. Phys. Lett.* **2009**, *94*. [[CrossRef](#)]
10. Klimov, V.I.; Mikhailovsky, A.A.; Xu, S.; Malko, A.; Hollingsworth, J.A.; Leatherdale, C.A.; Eisler, H.J.; Bawendi, M.G. Optical Gain and Stimulated Emission in Nanocrystal Quantum Dots. *Science* **2000**, *290*, 314–317. [[CrossRef](#)] [[PubMed](#)]
11. Larson, D.R.; Zipfel, W.R.; Williams, R.M.; Clark, S.W.; Bruchez, M.P.; Wise, F.W.; Webb, W.W. Water-soluble Quantum Dots for Multiphoton Fluorescence Imaging in vivo. *Science* **2003**, *300*, 1434–1436. [[CrossRef](#)] [[PubMed](#)]
12. Li, M.; Yu, X.-F.; Liang, S.; Peng, X.-N.; Yang, Z.-J.; Wang, Y.-L.; Wang, Q.-Q. Synthesis of Au-CdS Core-Shell Hetero-Nanorods with Efficient Exciton-Plasmon Interactions. *Adv. Funct. Mater.* **2011**, *21*, 1788–1794. [[CrossRef](#)]
13. Liu, W.; Howarth, M.; Greytak, A.B.; Zheng, Y.; Nocera, D.G.; Ting, A.Y.; Bawendi, M.G. Compact biocompatible quantum dots functionalized for cellular imaging. *J. Am. Chem. Soc.* **2008**, *130*, 1274–1284. [[CrossRef](#)] [[PubMed](#)]
14. Michalet, X.; Pinaud, F.F.; Bentolila, L.A.; Tsay, J.M.; Doose, S.; Li, J.J.; Sundaresan, G.; Wu, A.M.; Gambhir, S.S.; Weiss, S. Quantum dots for live cells, in vivo imaging, and diagnostics. *Science* **2005**, *307*, 538–544. [[CrossRef](#)] [[PubMed](#)]
15. Moreels, I.; Lambert, K.; Smeets, D.; de Muynck, D.; Nollet, T.; Martins, J.C.; Vanhaecke, F.; Vantomme, A.; Delerue, C.; Allan, G.; et al. Size-Dependent Optical Properties of Colloidal PbS Quantum Dots. *ACS Nano* **2009**, *3*, 3023–3030. [[CrossRef](#)] [[PubMed](#)]
16. Fedorov, A.V.; Baranov, A.V.; Inoue, K. Two-photon Transitions in Systems with Semiconductor Quantum Dots. *Phys. Rev. B* **1996**, *54*, 8627–8632. [[CrossRef](#)]
17. Rogach, A.L. *Semiconductor Nanocrystal Quantum Dots: Synthesis, Assembly, Spectroscopy and Application*; Springer: New York, NY, USA, 2008.
18. Nootz, G.; Padilha, L.A.; Olszak, P.D.; Webster, S.; Hagan, D.J.; van Stryland, E.W.; Levina, L.; Sukhovatkin, V.; Brzozowski, L.; Sargent, E.H. Role of Symmetry Breaking on the Optical Transitions in Lead-Salt Quantum Dots. *Nano Lett.* **2010**, *10*, 3577–3582. [[CrossRef](#)] [[PubMed](#)]
19. Trinh, M.T.; Sfeir, M.Y.; Choi, J.J.; Owen, J.S.; Zhu, X. A Hot Electron-Hole Pair Breaks the Symmetry of a Semiconductor Quantum Dot. *Nano Lett.* **2013**, *13*, 6091–6097. [[CrossRef](#)] [[PubMed](#)]
20. Rebane, A.; Drobizhev, M.; Makarov, N.S.; Wicks, G.; Wnuk, P.; Stepanenko, Y.; Haley, J.E.; Krein, D.M.; Fore, J.L.; Burke, A.R.; et al. Symmetry Breaking in Platinum Acetylide Chromophores Studied by Femtosecond Two-Photon Absorption Spectroscopy. *J. Phys. Chem. A* **2014**, *118*, 3749–3759. [[CrossRef](#)] [[PubMed](#)]
21. Michler, P. *Single Quantum Dots Fundamentals, Applications and New Concepts*; Springer: New York, NY, USA, 2003.
22. Vivas, M.G.; Cury, J.F.; Schiavon, M.A.; Mendonca, C.R. Two-Photon Absorption of ZnS Quantum Dots: Interpreting the Nonlinear Spectrum. *J. Phys. Chem. C* **2013**, *117*, 8530–8535. [[CrossRef](#)]
23. Li, X.P.; Embden, J.; Chon, J.W.M.; Gu, M. Enhanced two-photon absorption of CdS nanocrystal rods. *Appl. Phys. Lett.* **2009**, *94*. [[CrossRef](#)]

24. Makarov, N.S.; Lau, P.C.; Olson, C.; Velizhanin, K.A.; Solntsev, K.M.; Kieu, K.; Kilina, S.; Tretiak, S.; Norwood, R.A.; Peyghambarian, N.; et al. Two-Photon Absorption in CdSe Colloidal Quantum Dots Compared to Organic Molecules. *ACS Nano* **2014**, *8*, 12572–12586. [[CrossRef](#)] [[PubMed](#)]
25. Qu, Y.; Ji, W. Two-photon Absorption of Quantum Dots in the Regime of very Strong Confinement: Size and Wavelength Dependence. *J. Opt. Soc. Am. B* **2009**, *26*, 1897–1904. [[CrossRef](#)]
26. Padilha, L.A.; Nootz, G.; Olszak, P.D.; Webster, S.; Hagan, D.J.; van Stryland, E.W.; Levina, L.; Sukhovatkin, V.; Brzozowski, L.; Sargent, E.H. Optimization of Band Structure and Quantum-Size-Effect Tuning for Two-Photon Absorption Enhancement in Quantum Dots. *Nano Lett.* **2011**, *11*, 1227–1231. [[CrossRef](#)] [[PubMed](#)]
27. Efros, A.L.; Rosen, M. Quantum size level structure of narrow-gap semiconductor nanocrystals: Effect of band coupling. *Phys. Rev. B* **1998**, *58*, 7120. [[CrossRef](#)]
28. Dakovski, G.L.; Shan, J. Size dependence of two-photon absorption in semiconductor quantum dots. *J. Appl. Phys.* **2013**, *114*. [[CrossRef](#)]
29. Padilha, L.A.; Fu, J.; Hagan, D.J.; van Stryland, E.W.; Cesar, C.L.; Barbosa, L.C.; Cruz, C.H.B.; Buso, D.; Martucci, A. Frequency degenerate and nondegenerate two-photon absorption spectra of semiconductor quantum dots. *Phys. Rev. B* **2007**, *75*, 075325. [[CrossRef](#)]
30. Khatei, J.; Sandeep, C.S.S.; Philip, R.; Rao, K.S.R.K. Near-resonant two-photon absorption in luminescent CdTe quantum dots. *Appl. Phys. Lett.* **2012**, *100*. [[CrossRef](#)]
31. Pan, L.; Tamai, N.; Kamada, K.; Deki, S. Nonlinear optical properties of thiol-capped CdTe quantum dots in nonresonant region. *Appl. Phys. Lett.* **2007**, *91*. [[CrossRef](#)]
32. Padilha, L.A.; Fu, J.; Hagan, D.J.; van Stryland, E.W.; Cesar, C.L.; Barbosa, L.C.; Cruz, C.H.B. Two-photon Absorption in CdTe Quantum dots. *Opt. Express* **2005**, *13*, 6460–6467. [[CrossRef](#)] [[PubMed](#)]
33. Knowles, K.E.; Frederick, M.T.; Tice, D.B.; Morris-Cohen, A.J.; Weiss, E.A. Colloidal Quantum Dots: Think Outside the (Particle-in-a-)Box. *J. Phys. Chem. Lett.* **2012**, *3*, 18–26. [[CrossRef](#)]
34. Yu, W.W.; Qu, L.H.; Guo, W.Z.; Peng, X.G. Experimental Determination of the Extinction Coefficient of CdTe, CdSe, and CdS Nanocrystals. *Chem. Mater.* **2003**, *15*, 2854–2860. [[CrossRef](#)]
35. Vengrenovich, R.D.; Gudyma, Y.V.; Yarema, S.V. Ostwald ripening of quantum-dot nanostructures. *Semiconductors* **2001**, *35*, 1378–1382. [[CrossRef](#)]
36. Vivas, M.G.; de Boni, L.; Cooper, T.M.; Mendonca, C.R. Interpreting Strong Two-Photon Absorption of PE3 Platinum Acetylide Complex: Double Resonance and Excited State Absorption. *ACS Photonics* **2014**, *1*, 106–113. [[CrossRef](#)]
37. Sousa, J.C.L.; Vivas, M.G.; Ferrari, J.L.; Mendonca, C.R.; Schiavon, M.A. Determination of particle size distribution of water-soluble CdTe quantum dots by optical spectroscopy. *RSC Adv.* **2014**, *4*, 36024–36030. [[CrossRef](#)]
38. Wang, Y.; Liu, S. One-Pot Synthesis of Highly Luminescent CdTe Quantum Dots using Sodium Tellurite as Tellurium Source in Aqueous Solution. *J. Chil. Chem. Soc.* **2012**, *57*, 1109–1112. [[CrossRef](#)]
39. Kubin, R.F.; Fletcher, A.N. Fluorescence quantum yields of some rhodamine dyes. *J. Lumines* **1982**, *27*, 455–462. [[CrossRef](#)]



© 2017 by the authors. Licensee MDPI, Basel, Switzerland. This article is an open access article distributed under the terms and conditions of the Creative Commons Attribution (CC BY) license (<http://creativecommons.org/licenses/by/4.0/>).